Journal of
Materials Chemistry C

Materials for optical, magnetic and electronic devices

Accepted Manuscript

This article can be cited before page numbers have been issued, to do this please use: M. Lederer, M. Stremel, I. Pompermayer Machado, T. Förster, S. S. Razi, M. Suta and A. M. Kaczmarek, *J. Mater. Chem. C*, 2025, DOI: 10.1039/D5TC01916H.

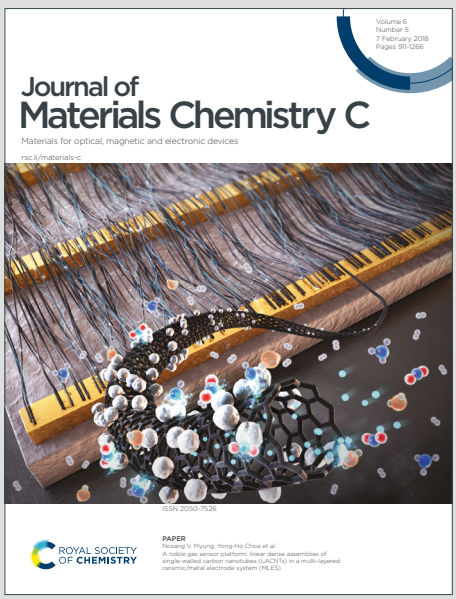

ROYAL SOCIETY OF CHEMISTRY

rsc.li/materials-c

Understanding the thermometric action of $LiLuF_4:Tm^{3+}$, Yb^{3+}

View Article Online
DOI: 10.1039/D5TC01916H

*Mirijam Lederer,[a] Maximilian Stremel,[b] Ian Pompermayer Machado,[a] Tom Förster,[b] Syed S. Razi,[a] Markus Suta *[b] and Anna M. Kaczmarek *[a]*

Received 00th January 20xx,
Accepted 00th January 20xx

DOI: 10.1039/x0xx00000x

While the classic Er^{3+}, Yb^{3+} upconversion couple with its background-free green emission from the two thermally coupled $^2H_{11/2}$ and $^4S_{3/2}$ levels of Er^{3+} is a "working horse" example for luminescent Boltzmann thermometry, the Tm^{3+}, Yb^{3+} couple is far from well established. The Tm^{3+}, Yb^{3+} system offers the intense $^3H_4 \rightarrow {}^3H_6$ electronic transition (800 nm) as a possible reference emission for UC thermometry in the NIR-I. However, so far the Tm^{3+}, Yb^{3+} thermometry system is not fully understood, limiting a possible application in medical/biological applications, as well as in nanoelectronics, nanophotonics and in general industrial settings. In this work, we demonstrate how to exploit the temperature-dependent multiphonon relaxation from the $^3F_3$ to the $^3H_4$ level of Tm^{3+} fed by energy transfer *via* Yb^{3+} giving rise to two emission lines at 680 nm and 800 nm. Taking $LiLuF_4$: 1%Tm, 30%Yb as a representative example compound, we have analyzed both micro- and nanocrystalline samples to elucidate the impact of surface-attached ligands with higher vibrational energies than the low cutoff phonon energies (~ 500 cm^{-1}) of the fluoride matrix itself. We show that Tm^{3+} can only work as a wide-range Boltzmann thermometer in microcrystalline, ligand-free samples with host compounds of sufficiently low cutoff phonon energies and its action is limited in nanocrystalline systems. A combination of experimental studies and kinetic modelling helps elucidate clear-cut guidelines and compare this UC system to the well-established working horse of Er^{3+}, Yb^{3+} in the performance as a luminescent thermometer.

Introduction

Temperature sensors are in high demand, as temperature is a fundamental parameter in multiple sectors such as industry, research and medicine.[1–5] The currently used techniques such as thermocouples and thermistors are inappropriate for some catalysis applications, micro- and nanofluids, micro- and nanoelectronics, as well as biological applications, as they require non-invasive, remote detection.[1–4,6,7] Thermometers that do not require calibration in every media and experimental setup are advantageous for *operando* applications.[8,9] (Nano)thermometry offers outstanding properties such as fast, remote, non-invasive, accurate, sensitive and reliable temperature readout of even fast-moving objects in strong electromagnetic fields.[7,10–13] Utilizing trivalent lanthanides (Ln^{3+}) as emissive ions for (nano)thermometry offers stable, narrow-band emissions that cover the whole electromagnetic spectrum over wide temperature ranges.[1,4,11,12] However, their respective energy levels are very complex ladder-like structures, resulting in equally sophisticated spectra, usually stemming from $4f^n$-$4f^n$ transitions. However, those $4f^n$-$4f^n$ electronic transitions are electric dipole-forbidden in centrosymmetric symmetries and only become partially allowed due to asymmetries within the crystal field surrounding the Ln^{3+}. This leads to the issue of generally weak emissions.

For some applications, it is of utmost importance to choose lanthanoid ions that exhibit bright emission lines in the biological window (BW) I (750 nm to 950 nm).[1,14–21] In those regions of the electromagnetic spectrum, absorption of overtone vibrations of *X*-H (*X* = C, N, O) groups from e.g., water or lipids is still rather high and can thus, potentially quench the lanthanide-based luminescence.[10,22,23] This is important as the only induced electric dipolar nature of the $4f^n$-$4f^n$ electronic transitions and the connected low absorption cross sections generally lower the overall brightness of the photoluminescence of the trivalent lanthanoid ions. A common beneficial approach for luminescent thermometry is the usage of an energy transfer couple for upconversion (UC).[4,24,25] In this approach, a well-absorbing sensitizer like Yb^{3+} is excited directly and then transfers its energy to the activator, e.g. Er^{3+} or Tm^{3+}. Besides a comparably large absorption cross-section of Yb^{3+} compared to other trivalent lanthanoid ions offers the additional benefit of excitation in the NIR I, which is relatively cheap. Moreover, NIR-excited UC emission is typically background-free, which limits potentially arising systematic errors in the calibration procedure of a luminescent

[a] *NanoSensing Group, Department of Chemistry, Ghent University, Krijgslaan 281-S3, 9000 Ghent, Belgium. E-mail: anna.kaczmarek@ugent.be*

[b] *Inorganic Photoactive Materials, Institute of Inorganic Chemistry, Heinrich Heine University Düsseldorf, Universitätsstraße 1, 40225 Düsseldorf, Germany. E-mail: markus.suta@hhu.de*

† Electronic Supplementary Information (ESI) available: HRTEM images, histograms, SEM images, STEM images and EDX maps, EDX line scans, PXRD patterns, FFT patterns, ICP-OES results, (high temperature) photoluminescence measurements and respective calculations, decay times, FTIR spectra. See DOI: 00.0000/00000000.

View Article Online
DOI: 10.1039/D5TC01916H

thermometer. UC itself is beneficial as it is considered relatively background free and therefore results in improved accuracy in luminescence thermometry.[10,26,27] A particularly popular and simple approach in UC thermometry with Ln^{3+} is ratiometric thermometry.[1,4,10,12] Here, the intensities of two radiative transitions are compared to each other as the intensity ratio changes with temperature. The parameter of that ratio is commonly referred to as the luminescent intensity ratio (LIR) or Delta (Δ).[10,28] For single-ion narrow-line emitters such as Er^{3+} with two thermally coupled radiatively decaying excited levels, the LIR should follow Boltzmann's law.[3,4,16,27,29]

For all kinds of applications, a high chemical, mechanical and thermal stability is important. For UC with trivalent lanthanoid ions, a low phonon energy is favorable to limit nonradiative relaxation pathways by means of the energy gap law that otherwise lower the total decay times of the excited $4f^n$ levels.[10,30,31] $LiLuF_4$ as host material is an excellent choice, as it has a low cutoff phonon energy (~ 550 cm^{-1})[32,33], but also it is known to be stable for high temperature thermometry.[30,34] Especially for UC systems it is also notable that $LiLuF_4$ has shown high absolute UC quantum yields (QY), exceeding 5%.[35] Additionally, $LiLuF_4$ nanocrystals (NCs) can be easily synthesized with high degrees of crystallinity and high reproducibility *via* a thermal decomposition route leading to different morphologies, including core-shell structures by means of co-precipitation and thermal decomposition synthesis routes.[30,33,34]

In this work, we would like to build upon the success of the Er^{3+}, Yb^{3+} upconversion system and investigate the possibilities to use the Tm^{3+}, Yb^{3+} upconversion couple as an alternative luminescent thermometry system. This couple is an interesting pair due to the possibility to utilize both blue and NIR emission by cooperative energy-transfer upconversion *via* the Yb^{3+} ions in fluorides. Unlike Er^{3+}, Tm^{3+} with its $4f^{12}$ configuration only has a limited number of resulting spin-orbit levels, which are often energetically isolated according to the Dieke-Crosswhite diagram.[36] Accordingly, classic Boltzmann thermometry exploiting energy gaps Δ*E* in the order of the desired thermal energy k_BT to be probed is not straightforward with this emitter.[9,29] Generally, Tm^{3+}, Yb^{3+} systems are well-suited candidates for UC thermometry, as they offer bright emissions in the visible and NIR range.[15,37–41] Up to date, not much work has been devoted to the underlying mechanism of thermal coupling among excited levels of Tm^{3+}.[4,7,12,14,42] The intensity ratio of the $^3F_{2,3} \rightarrow {}^3H_6$-based emission at 680 nm and $^3H_4 \rightarrow {}^3H_6$-based emission at 800 nm Tm^{3+}, Yb^{3+} system could be potentially considered thermally coupled, as the respective excited energy levels are separated by around $\Delta E \approx 1800$ cm^{-1}.[9,43] In this work, however, we demonstrate the difficulties in using this simplistic approach in the case of nanocrystalline fluorides with surface-attached ligands and their connected higher energetic vibrational modes.[29] To date publications on the Tm^{3+}, Yb^{3+} UC system in both Na^+- and Li^+- containing fluoride based host compounds (in micro-and nanocrystalline samples) have only scarcely considered the mechanism of this luminescence system yet this knowledge plays an important role for applied thermometry.[9,29,44–46] In this work, we propose temperature-activated cross-relaxation and consequent quenching of emission intensity as well as non-radiative deactivation as mechanisms that are likely prominent in the Tm^{3+}, Yb^{3+} system. We present a theoretically motivated explanation based on $LiLuF_4$:1%Tm^{3+},30%Yb^{3+} nano- and microcrystals for ratiometric UC thermometry with this couple of lanthanoid ions. Additionally, we have also investigated the influence of growing an inert $LiYF_4$ shell around the $LiLuF_4$ nanocrystalline core on its thermometric behavior. The samples were characterized by powder X-ray diffraction (PXRD), high-resolution transmission electron microscopy (HRTEM), scanning electron microscopy (SEM), fast Fourier transform (FFT) patterns, scanning transmission electron microscopy (STEM) and energy dispersive X-ray (EDX) mapping as well as inductively coupled plasma optical emission spectroscopy (ICP-OES) to ensure that samples of high quality were obtained. Afterwards, extensive temperature-dependent steady-state and time-resolved luminescence were performed to ensure the correct modelling *via* extensive data curation. This guides the consequent modelling of the UC thermometry with a Tm^{3+}, Yb^{3+} system relying mainly on multi-phonon relaxation not only in the discussed region of the electromagnetic region, but also enable further developments and understanding of Tm^{3+}, Yb^{3+} systems working in other regions of the electromagnetic region.

Experimental Section

Synthesis procedure

View Article Online
DOI: 10.1039/D5TC01916H

All chemicals were commercially purchased and used without further purification if not indicated otherwise. For the solid-state synthesis, the saturated NH_4F was purchased from Thermo Scientific (purity: 98%+) and the $LiBF_4$ was obtained from BLD Pharm (purity: 99.96%).

Synthesis of trifluoroacetate precursors for thermal decomposition synthesis

RE$(CF_3COO)_3$ with *RE* = Lu, Yb and Tm were prepared according to the following protocol.[30] An appropriate amount of the corresponding of Ln_2O_3 was placed in a 40 mL glass vial that was filled to one-third with deionized (DI) water and sonicated for 2 min in an ultrasound bath. After that, the same volume of trifluoroacetic acid was added to the mixture under the fume hood. The mixture was placed in a sand bath set at 95 °C for at least 48 h. CF_3COOLi precursors were prepared using the same method, but LiOH were used instead of Ln_2O_3. After at least 48 h, a powder was collected.

Thermal decomposition synthesis of $LiLuF_4$:Tm, Yb core nanocrystals

The synthesis was previously reported by some of us[30,34] and makes use of the above described RE$(CF_3COO)_3$ precursors, dissolved in high boiling point solvents. 6 mL of oleic acid, 2 mL of 1-octadecene, 2 mL of oleylamine, 1 mmol CF_3COOLi, and 1 mmol RE$(CF_3COO)_3$ (with *RE* = Lu, Yb and Tm in appropriate amounts) were added to a three-neck glass flask. First, the mixture was heated to 120 °C under vacuum and kept at this temperature for 30 min. After this initial step, the atmosphere was changed to N_2 gas flow, and the mixture was stirred at 120 °C for 30 min. The last step was heating to 320 °C under nitrogen for 40 min. Finally, the mixture was cooled to room temperature. The resulting nanocrystals were washed three times with acetone after redispersing them in cyclohexane and collected by centrifuging.

Co-precipitation synthesis of inert LiYF4 shell around $LiLuF_4$:Tm, Yb core nanocrystals

The synthesis of the undoped $LiYF_4$ inorganic shell around the doped $LiLuF_4$:Tm^{3+}, Yb^{3+} core nanocrystals was also already described in a previous work of some of us.[34] For that, 5 mL of oleic acid, 5 mL of 1-octadecene and 1 mmol YCl_3 were mixed in a three-neck flask. This mixture was placed under vacuum at 120 °C for 2 h until the chlorides were fully dissolved. After that, the mixture was cooled to 50 °C and the already prepared $LiLuF_4$:Tm^{3+}, Yb^{3+} core nanocrystals, dispersed in 5 ml cyclohexane, were injected into the reaction. After that, the cyclohexane was evaporated under vacuum at 120 °C for 30 min. During the evaporation step, 2 mmol NH_4F and 1.5 mmol LiOH were weighted off and separately dissolved in 2–3 mL of methanol in an ultrasound bath for at least 30 min. Afterwards, the mixture was cooled to 50 °C under nitrogen flow. The dissolved NH_4F and LiOH were quickly mixed together and injected into the three-neck flask. For the necessary nucleation step, the flask was kept at 120 °C for 30 min after which the 5 ml methanol was evaporated at 120 °C for 30 min under vacuum. Next, the mixture was heated to 320 °C under nitrogen and was kept there for 1 h. Lastly, the reaction was cooled to room temperature. To purify the nanocrystals, they were washed and precipitated with cyclohexane and acetone, as already described above.

Oleate ligand removal from the nanocrystals

The oleate-capped core and core-shell nanocrystals were dispersed in 5 ml of cyclohexane and mixed with 10 mL DI water. Afterwards, 0.1 molar HCl was added to maintain pH = 4. This mixture was sonicated for 1 h. In that process, the carboxylate groups of the oleate ligand were protonated and the oleic acid was consequently separated from the nanocrystals in the two phases of the reaction. The now uncapped nanocrystals were precipitated in ethanol, centrifuged and then washed two times in DI water. Afterwards, the samples were dried at 80 °C overnight.

Autoclave synthesis of $LiLuF_4$:Tm, Yb microcrystals

The synthesis of the $LiLuF_4$ microcrystals was inspired by Zheng et al.[47] For that, 1 mol of $Ln(NO_3)_3$ (with Ln = Tm, Yb and Lu) in appropriate ratios were mixed with 2 ml of DI water in an ultrasound bath until fully dissolved. Afterwards, 0.05 mol of EDTA was mixed with 40 ml of DI in a round bottom flask and the dissolved nitrate salts were added. The mixture was vigorously stirred for 60 min after which 1 mol of NH_4F dissolved in 12 ml DI and 1 mol of LiF dissolved in 8 ml DI were added. After continued stirring for 20 min, the mixture was transferred to a Teflon-lined autoclave. The autoclave was placed in an oven and heated to 180 °C for 24 h after which it was cooled down naturally and collected with DI. Subsequent steps were one to two washing steps with ethanol, after which the microcrystals were dried at 60°C.

Solid-state synthesis of $LiLuF_4$:Tm, Yb microcrystals

View Article Online
DOI: 10.1039/D5TC01916H

$LiLuF_4$:1%Tm^{3+} ,30% Yb^{3+} microcrystals were prepared *via* a solid-state synthesis by dissolving the respective oxides Ln_2O_3 in concentrated hydrochloric acid in stoichiometric amounts. The solvent of the thus obtained transparent solution was evaporated. The resulting residue was re-dissolved in DI water. Upon addition of a saturated NH_4F solution, a colourless precipitate could be isolated, dried at 80 °C overnight and was decomposed at 375 °C under a constant N_2 flow for 5 h to yield the pure rare earth fluorides. The resulting mixture was first heated at 120°C, re-mixed with excess NH_5F_2 and re-heated at 400 °C overnight. Finally, the powder was treated with $LiBF_4$ at 500°C for 12 h over a bed of NH_5F_2.

Characterization techniques

Transmission Electron Microscope (TEM) images were obtained with a JEOL JEM-2200FS TEM, operated at 200 kV equipped with a Cs corrector. Scanning TEM (STEM) images were obtained with the same instrument utilizing the high-angle annular dark field (HAADF) and bright field (BF) detector. STEM EDX mapping was performed *via* energy dispersive X-ray (EDX) spectroscopy in HAADF-STEM mode. All TEM samples were prepared on a 300-mesh holey carbon copper grid. The nanocrystals were applied *via* placing one or two drops of a DI water suspension of nanocrystals with their ligands removed on the grid and drying at room temperature afterwards on a filter paper. Particle sizes and consequently histograms were obtained *via* the softwares ImageJ and Origin. The sizing was performed with at least 100 particles on overview TEM images. STEM images, EDX maps and line scans were obtained using the program Analysis Station from JEOL. The data for the line scans was smoothed in Origin *via* a 15-point Savitzky-Golay function. Powder X-Ray Diffraction (PXRD) patterns were recorded with a benchtop Rigaku Miniflex Rigaku Diffractometer. The patterns were recorded from angles of 2ϑ = 15° to 2ϑ = 60°. The Rietveld refinement was performed with Topas, refining the lattice parameters freely using the Thompson-Cox-Hastings profile function.[58] The diffractogram was plotted using OriginPro 2024 software. The material composition was determined by inductively coupled plasma optical emission spectroscopy (ICP-OES) using an iCap 7000 duo (ThermoFisher). Scanning electron microscopy (SEM) measurements were performed using a FEI Quanta 200 FSEM. Photoluminescence (PL) spectra were recorded using an Edinburgh Instruments FLS1000 UV-Vis-NIR spectrofluorometer that was equipped with a Hamamatsu R928P photomultiplier tube (PMT, Hamamatsu, Shizuoka, Japan). For measurements in the NIR range a Hamamatsu R5509–72 photomultiplier was used to detect emission. The excitation source was a power-tuneable continuous wave (CW) laser (power limit: P_{max} = 2 W, Livingston, UK) with an excitation wavelength of 975 or 690 nm. Time-resolved measurements were performed using the same equipment, using an external modulator. High temperature PL measurements were performed in powder after ligand removal in a Linkam (Surrey, UK) THMS600 Microscope Stage with ±0.1 K temperature stability. The Linkam stage was placed inside the FLS1000 setup and the spectra were recorded from 298.15 to 498.15 K in steps of 20 K. For the low (77 K) to high (870 K) temperature measurements of the $LiLuF_4$:1%Tm,30%Yb NC and MC an Edinburgh Instruments FLS1000 UV-Vis-NIR spectrofluorometer equipped with a double excitation and emission monochromators in Czerny-Turner configuration and a thermoelectrically cooled (−253 K) photomultiplier tube PMT-980 (Hamamatsu, Shizuoka, Japan) and a 975 nm CW power-tunable laser (power limit: P_{max} = 400 mW, Livingston, UK) in a Linkam stage with optical fibre bundles. In order to compare the measurements, the settings for each measurement (step size and dwell time) were kept equal. The excitation source and wavelength as well as observation wavelength/peak are specified in the respective Figure caption. Thermometrically relevant data of micro- and nanocrystals was plotted using the TeSen software, as described above.[48] The solid-state sample, modelling and calibration data was analyzed using OriginPro 2024.

Theoretical Background

In **Figure 1** the proposed energy diagram for a Tm^{3+}, Yb^{3+} UC system excited into the $^2F_{5/2}$ energy level of Yb^{3+} at 975 nm is shown with the observed emission of the Tm^{3+} centered at 680 nm stemming from the $^3F_3 \rightarrow {}^3H_6$ electronic transition (red arrow) and the 800 nm emission stemming from the $^3H_4 \rightarrow {}^3H_6$ electronic transition (brown arrow). The $^3H_4 \rightarrow {}^3H_6$ electronic transition has a high intensity based on its Judd-Ofelt allowed character and the energetically rather isolated nature of the excited $^3H_4$ level limits nonradiative relaxation.[49–51] Additonally, upconversion in the Tm^{3+}–Yb^{3+} couple can be efficiently achieved by a sequential energy transfer upon excitation of two Yb^{3+} ions at 980 nm that transfer their energy to Tm^{3+}. The process is schematically depicted in Figure 1. In the first instance, energy transfer from Yb^{3+} to Tm^{3+} leads to population of the $^3H_5$ level

View Article Online
DOI: 10.1039/D5TC01916H

that may additionally nonradiatively relax to the $^3F_4$ level. From there, energy transfer from a second excited Yb^{3+} ion ultimately leads to feeding of the $^3F_{2,3}$ levels of Tm^{3+} *via* upconversion. It is well established that both nonradiative depopulation of the $^3F_2$ electronic level and Tm^{3+}-Tm^{3+} cross-relaxation populate the $^3H_4$ electronic level efficiently, enhancing the brightness of the emission centered around 800 nm.

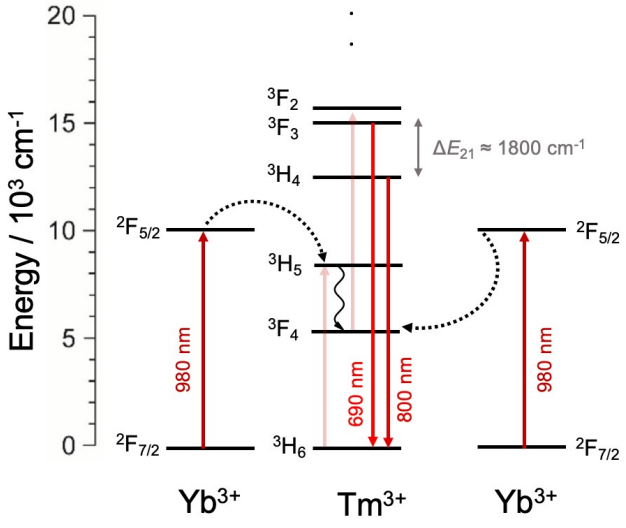

Figure 1: Energy level diagram for the Tm^{3+}, Yb^{3+} thermometric system upon pumping Yb^{3+} at 975 nm (black arrow). Radiative transitions used for ratiometric thermometry are the $^3F_3 \rightarrow {}^3H_6$ electronic transition (680 nm emission, red arrow) and the $^3H_4 \rightarrow {}^3H_6$ electronic transition (800 nm emission, brown arrow) of Tm^{3+}. The 640 nm emission of Tm^{3+} stemming from the $^1G_4 \rightarrow {}^3F_4$ is also indicated in blue.

It is in principle a possibility that the $^3F_{2,3}$ and $^3H_4$ levels could be thermally coupled, allowing for classic ratiometric Boltzmann thermometry when using the emission lines of Tm^{3+} at 680 nm and 800 nm. However, the mutual energy gap between these two levels is around 1800 cm^{-1}, which means that non-radiative absorption (and thus, Boltzmann equilibrium) is only expected at elevated temperatures as cutoff phonon modes ($\hbar\omega_{cut} \approx 550$ cm^{-1}) need to be thermally excited.[45] Theoretically, the $^3H_4 \rightarrow {}^3H_6$ transition is not expected to be easily thermally quenched at low temperatures, as the energy difference from the $^3H_4$ to the $^3H_5$ electronic energy level is about 4000 cm^{-1}, therefore requiring roughly 8 phonons to bridge the energy difference between these levels in $LiLuF_4$.[45] At elevated temperatures, thermal population of the low-energetic cutoff phonon modes can, however, accelerate the nonradiative relaxation process. Nevertheless, it is known that surface quenching over surface-attached ligands with *X*-H (*X* = C, N, O) groups bridge the energy gap even resonantly.[27,46,52,53] Thus, the thermometrically relevant energy levels $^3H_4 = |1\rangle$ and $^3F_3 = |2\rangle$ of Tm^{3+} within this work are governed by the following rate equations:

$$\dot{n}(\,^3F_3) = -k_{2r}n(\,^3F_3) - k_{nr}^{em}(T)n(\,^3F_3) + k_{nr}^{abs}(T)n(\,^3H_4) - k_{nr}^{xr}n(\,^3F_3) \quad \text{Equation 1}$$

$$\dot{n}(\,^3H_4) = -k_{1r}n(\,^3H_4) - k_{nr}^{abs}(T)n(\,^3H_4) + k_{nr}^{em}(T)n(\,^3F_3) - k_{quench}n(\,^3H_4) \quad \text{Equation 2}$$

with k_{jr} as the radiative decay rate constants of state $|j\rangle$ (j = 1, 2; see above), $k_{nr}^{abs}(T)$ and $k_{nr}^{em}(T)$ as the temperature-dependent non-radiative absorption and emission rates thermally coupling the $^3H_4 = |1\rangle$ and $^3F_3 = |2\rangle$ levels of Tm^{3+}. k_{nr}^{xr} is the cross-relaxation rate additionally depopulating the $^3F_{2,3}$ levels at higher Tm^{3+} concentrations due to the energy transfer process [Tm1, Tm2]: [$^3F_3$, $^3H_6$] → [$^3F_4$, $^3H_5$]. At the considered low activator fractions within this work (especially in the microcrystalline samples), however, cross-relaxation of the $^3F_3$ level of Tm^{3+} will only have minor relevance and may be neglected. Finally, k_{quench} denotes the rate representing any nonradiative quenching processes of the $^3H_4$ level.

Results and Discussion

Nanocrystalline (NC) and microcrystalline (MC) particles with the formula $LiLuF_4$:Tm^{3+}, Yb^{3+} with various ratios of Tm^{3+} and Yb^{3+} were grown and fully characterized. HRTEM images (see **Figure 2**) show a homogeneous, monodisperse size distribution of the nanocrystals, as shown exemplarily for the $LiLuF_4$:1%Tm,30%Yb NCs in the histograms in **Figure S1** (a). These results were expected, as these synthesis have previously been reported by some of us in other works.[30,34] HRTEM images of the other activation ratios are shown in **Figure S2** in the SI.

SEM images of the respective $LiLuF_4$:Tm^{3+}, Yb^{3+}: (a, e) 1% Tm^{3+}, 30% Yb^{3+}; (b, f) 1% Tm^{3+}, 35% Yb^{3+}; (c, g) 1.5% Tm^{3+}, 30% Yb^{3+}; (d, h) 1.5% Tm^{3+}, 35% Yb^{3+}: MCs are depicted in the SI in **Figure S3**. The composition of the $LiLuF_4$:1%Tm,30%Yb core and core-shell (CS) NCs and MCs were investigated *via* ICP-OES. Their respective lanthanide activation ratios are shown in **Table S1** in the SI, confirming that the synthetic and expected lanthanide percentages are in good agreement.

View Article Online
DOI: 10.1039/D5TC01916H

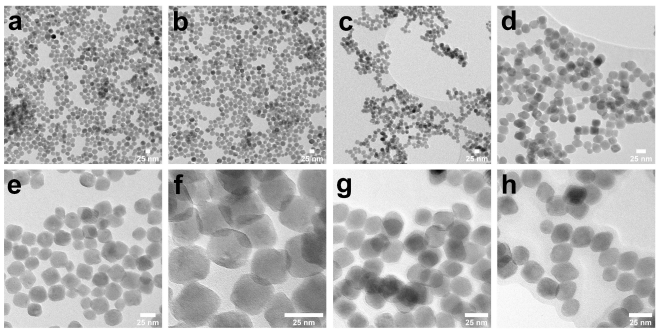

Figure 2: TEM images of $LiLuF_4$:Tm^{3+}, Yb^{3+} core nanocrystals with the following lanthanide ratios: (a, e) 1% Tm^{3+},30% Yb^{3+}; (b, f) 1% Tm^{3+}, 35% Yb^{3+}; (c, g) 1.5% Tm^{3+}, 30% Yb^{3+}; (d, h) 1.5%Tm,35%Yb. The top images show a general overview of the nanocrystals, while the bottom images are at higher magnification. The scale bar is 25 nm for all images.

HRTEM images of core-shell LiLuF4: 1% Tm^{3+}, X% Yb^{3+}@$LiYF_4$ nanocrystals (with X=25, 30 and 35) are shown in **Figure S4** in the SI, the histogram of the $LiLuF_4$: 1% Tm^{3+}, 30% Yb^{3+}@$LiYF_4$ CS NCs are shown in **Figure S1** (b). The increase in size after shelling is consistent with earlier findings that some of us reported for similar $LiLuF_4$@$LiYF_4$ type of nanocrystals, indicating a successful shell formation of around 2 nm in thickness over the whole surface of the core NCs.[30,34] The crystallinity of the $LiYF_4$ shell was investigated *via* FFT patterns on the HRTEM images of the $LiLuF_4$: 1% Tm^{3+}, 30% Yb^{3+}@$LiYF_4$ nanocrystals, as shown in **Figure S5** in the SI. They indicate clearly that both the core and the shell region are highly crystalline. Additionally, the integrity of the inert shell was investigated with STEM images and EDX maps with respective line scans for the $LiLuF_4$: 1% Tm^{3+}, 30% Yb^{3+}@$LiYF_4$, presented in the SI in **Figure S6, S7** and **S8**. It was important to prove that no significant ion intermixing between the core and shell ions is taking place and the emissive ions in the core are properly shielded by the inert shell. As already suggested in previous works by us, ion diffusion in Li^+ containing host matrices cannot be prevented with homogenous core-shell geometries.[34] Rather, a heterogenous core-shell geometry with a respective interface such as $LiLuF_4$@$LiYF_4$ is necessary to prevent significant ion migration.

The presented core-shell nanocrystals show a regular size distribution, with an inert shell and interface region with minimal ion migration. Besides the morphology and size, also the crystallinity and correct crystal phase of the materials is of great importance, as the crystal field around the luminescent Ln^{3+} is essential for bright emission intensity and limited non-radiative losses.[27]

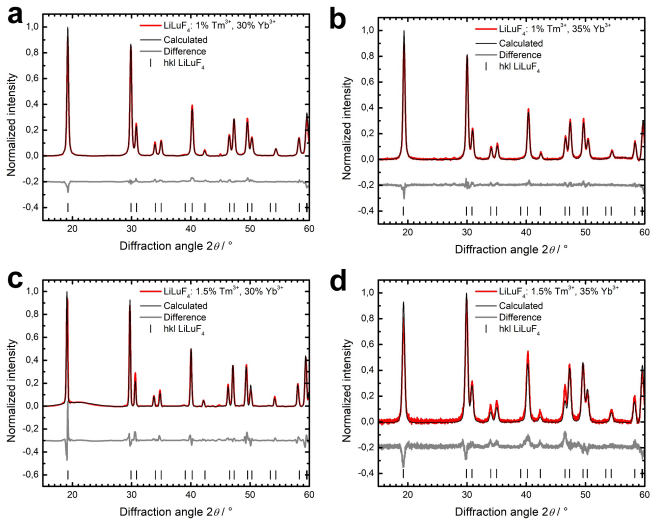

Figure 3: Rietveld refinement of PXRD patterns (Cu K_α radiation) of $LiLuF_4$:Tm^{3+}, Yb^{3+} NCs with different activator ratios of Tm and Yb with $LiLuF_4$ (#PDF 00-027-1251)[54]: (a) 1% Tm^{3+}, 30% Yb^{3+}, (b) 1% Tm^{3+}, 35% Yb^{3+}, (c) 1.5% Tm^{3+}, 30% Yb^{3+}, (d) 1.5% Tm^{3+}, 35% Yb^{3+}.

The Rietveld refinement of the PXRD patterns for the $LiLuF_4$:Tm^{3+}, Yb^{3+} NCs are shown in **Figure 3**: (a) 1% Tm^{3+}, 30% Yb^{3+}; (b) 1% Tm^{3+}, 35% Yb^{3+}; (c) 1.5% Tm^{3+}, 30% Yb^{3+} and (d) 1.5%Tm,35%. They are in good agreement with the 39563 ICSD reference data for $LiLuF_4$ (#PDF 00-027-1251).[54] The slight differences between the refined and detected intensities of the Bragg reflections are most likely caused by the reflection geometry of the Miniflex benchtop XRD, the related low goniometer radius of only 150 mm, and consequent texture effects based on the sample preparation. However, for a determination of the actually relevant lattice parameters, the position of the Bragg reflections is more decisive, for which that data quality is already sufficient.

Respective PXRD patterns of the respective NC and MC samples are depicted and discussed in the SI in **Figure S9** (NCs core), **Figure S10** (MCs) and **Figure S11** (NCs CS). They show that with increasing activation percentage of Yb^{3+}, the reflection position is shifting to higher angles of 2θ, whereas with increasing Tm^{3+} amount, the reflection position is shifting to lower angles of 2θ. As can be deducted from **Table S2**, with higher doping percentages, the unit cell expands. For the $LiLuF_4$: 1.5% Tm^{3+}, 35% Yb^{3+} it relaxes again, indicating that Tm and Yb are not incorporated into the lattice as defects anymore. For the $LiLuF_4$: 1% Tm^{3+}, 30% Yb^{3+} it can be

View Article Online
DOI: 10.1039/D5TC01916H

concluded that both Tm and Yb are not clustered in the NCs and MCs and the unit cell expands and contracts accordingly to doping percentages.

Photoluminescence

The photoluminescence emission maps of $LiLuF_4$:1%Tm,30%Yb NCs and MCs, upon excitation at 975 nm, are depicted in **Figure 4** (a, core NCs), (c, MCs), (e, CS NCs). The thermal response of other ratios of Tm^{3+} and Yb^{3+} in $LiLuF_4$ nano- and microcrystals are compiled in **Figure S12** (NCs) and **Figure S13** (MCs). Because absolute intensities are prone to many experimental errors and statements about thermal behaviour, a given transition should be rather related to time-resolved measurements.[8,30,34,55,56] The luminescent intensity ratio $\Delta = I(680\ nm)/I(800\ nm)$ shows a general increase with increasing temperatures in microcrystalline as well as core-only and core-shell nanocrystals. This finding could imply thermalization between the $^3F_{2,3}$ and $^3H_4$ levels of Tm^{3+}, respectively.

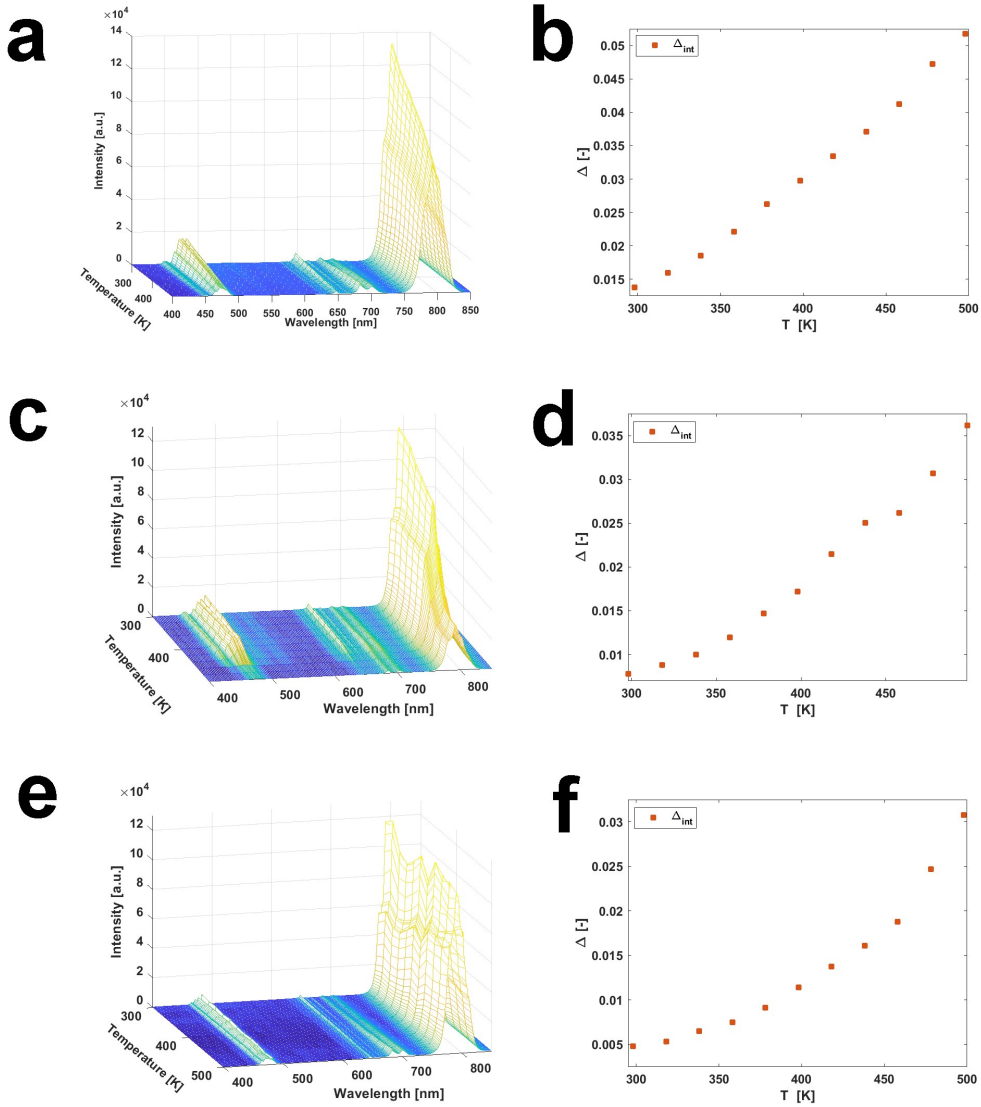

Figure 4: Photoluminescence emission maps of $LiLuF_4$:1%Tm,30%Yb (a) core-only NCs, (c) MC, and (e) core-shell $LiLuF_4$:1%Tm,30%Yb @$LiYF_4$ NCs excited with 975 nm in a temperature range from 298.15 to 498.15 K. The respective luminescent intensity ratio Δ (b, d and f) was calculated using the ratio of the area under the peak for the $^3F_{2,3} \rightarrow {}^3H_6$ electronic transition (emission at 680 nm) and the $^3H_4 \rightarrow {}^3H_6$ electronic transition (emission at 800 nm) of Tm^{3+}. Data of other ratios of core and core-shell nanocrystals and microcrystalline samples are shown in the SI.

View Article Online
DOI: 10.1039/D5TC01916H

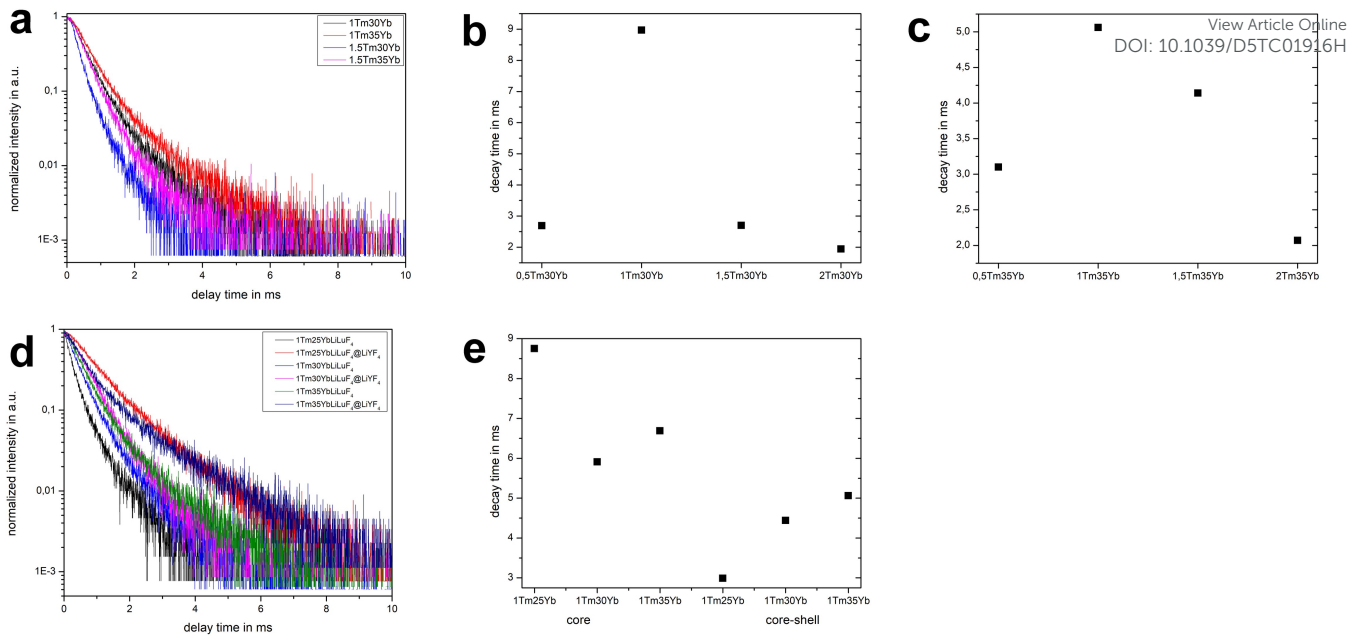

Figure 5: Normalized luminescence decay curves of the $^3H_4 \rightarrow {}^3H_6$-based emission ($\lambda_{em}$ = 800 nm) in $LiLuF_4$:Tm, Yb nanocrystals (λ_{ex} = 975 nm, T = 298.15 K). (a) Time-resolved luminescence of core-only $LiLuF_4$:*X*%Tm,*Y*%Yb NCs with X = 1, 1.5 and Y = 30, 35 (b) compiles the decay times for the NCs with 30% Yb while (c) shows the decay times for 35% Yb NC. (d) shows the decay curves for of $LiLuF_4$:Tm, Yb (@$LiYF_4$) core and core-shell NCs, excited with 975 nm at room temperature range (298.15 K), observed at 800 nm ($^3H_4 \rightarrow {}^3H_6$ electronic transition of Tm). The curves are normalized to the respective maximum value; (e) shows the respective decay times and trends for the core and core-shell NCs. Respective decay curves are shown in the SI (Figure S14).

However, fits to a Boltzmann-type behaviour in the regarded temperature range between 300 K and 500 K were not successful and severely underestimated the expected mutual energy gap of ΔE = 1700 cm^{-1} between the $^3F_{2,3}$ and $^3H_4$ levels. Consequently, it must be concluded that thermal equilibrium is not sustained within that temperature range for the regarded activated core and CS NCs and MCs.

For a better understanding of the excited-state dynamics and a potential impact of cross-relaxation, time-resolved luminescence decay curves of the $^3H_4 \rightarrow {}^3H_6$-based emission of the core NCs were acquired at room temperature (see **Figure 5 (a) to (c)**). The results are summarized for selected samples in **Table S3** in the SI. Other activation ratios are shown in **Figure S14** and summarized in **Table S4**. In all regarded cases, the Yb^{3+} ions were excited at 975 nm, which leads to the observation of an initial rise component in the luminescence decay traces. In addition, a higher Tm^{3+} content in the core-only NCs shows a general decrease of the average decay time above 1 mol%, which suggests an alternative quenching pathway for the $^3H_4$ level in the $LiLuF_4$:Tm^{3+}, Yb^{3+} NCs. Multiphonon relaxation can be a severe quenching mechanism for a NIR emitter such as Tm^{3+}. For example, the $^3H_4$-$^3F_4$ energy gap of around 6800 cm^{-1} can be resonantly bridged by two O–H stretching vibrational modes, while the $^3H_4$-$^3H_5$ energy gap of around 4200 cm^{-1} may be resonantly bridged by energy transfer to a C–H stretching (ca. 2800 cm^{-1}) and bending (ca. 1400 cm^{-1}) vibration. To investigate that reasoning, FTIR measurements were performed. The respective FTIR spectra are shown in **Figure S15**. FTIR spectra indicate the presence of the discussed organic groups on the surface for both nano-and microcrystalline samples, even after ligand removal.

To investigate concentration-dependent Tm^{3+}-Tm^{3+} cross-relaxation rates and thermalization dynamics, additional time-resolved luminescence decay curves of the $^3F_{2,3} \rightarrow {}^3H_6$-based emission of the core NCs were acquired at room temperature. In **Figure S16a** they are presented, the respective values in **Table S5**. All curves were fitted to biexponential decay models, but despite the high quality of the fitting (R^2 = 0.99), there are deviations between the experimental data points and the fitted curves, especially at longer times, indicating a more complex

View Article Online
DOI: 10.1039/D5TC01916H

deactivation pathway of the $^3F_3$ level. Nonetheless, by only varying the Tm^{3+} concentration from 0.5 to 2.0%, a clear decrease in the calculated average lifetimes is detectable (Table S5), which is a strong indicator that Tm–Tm cross relaxation is a significant quenching pathway. To verify if this is not a feature of the NC systems, $^3F_{2,3} \rightarrow {}^3H_6$ decay curves were also measured for the $LiLuF_4$:1% Tm^{3+}, 30% Yb^{3+} solid-state sample (Figure S16b). For the same 1% Tm^{3+}, 30% Yb^{3+} nominal activator concentrations, the NC and microcrystalline solid-state materials exhibit the same decay profile, further evidencing that Tm–Tm cross relaxation is an intrinsic deactivation pathway for the $^3F_{2,3}$ levels in $LiLuF_4$:Tm^{3+}, Yb^{3+} systems regardless of the particle size.

Thus, while the $^3F_3$ level can be effectively depopulated by cross-relaxation at higher Tm^{3+} contents (both in NCs and MCs), the $^3H_4$ level can be efficiently depopulated by multiphonon relaxation due to the high vibrational energies of functional groups of the surface-attached ligands in nanocrystalline $LiLuF_4$. This quenching pathway apparently becomes more probable at higher Tm^{3+} contents due to an expectedly higher probability of located Tm^{3+} ions in the vicinity of the surface of the NCs. The overall impact on the luminescent intensity ratio will thus depend on the mutual interplay of these two depopulation pathways. Crucially, both quenching mechanisms consequently pose a general limitation onto using Tm^{3+} as a candidate for ratiometric thermometry with that concept since they diminish the overall achievable brightness[10,22] and thus, signal-to-noise ratio of the two relevant emission lines at around 680 nm ($^3F_3 \rightarrow {}^3H_6$) and 800 nm ($^3H_4 \rightarrow {}^3H_6$). The proposed additional quenching pathways (cross-relaxation and multi-phonon relaxation) also allow to explain the qualitative differences between the detected Delta parameter (Δ) in nano- and microcrystalline $LiLuF_4$:1%Tm,30%Yb (see **Figure 4** (b) and (d)). As ligand-induced quenching depopulates the lower energetic $^3H_4$ level in the nanocrystalline systems efficiently, the overall $\Delta = I_{680}/I_{800}$ becomes larger compared to a microcrystalline sample, in which merely the lower energetic cutoff phonon modes of $LiLuF_4$ ($\approx 550\ cm^{-1}$)[30] are relevant. In the core-shell NCs (see **Figure 5** (e) to (f)), the situation is comparable to the MC system. In addition, cross-relaxation of the $^3F_3$ level becomes an alternative critical quenching pathway at higher Tm^{3+} contents, which is concentration-dependent.

In all three considered cases (core-only NCs, MCs and CS NCs), these two quenching mechanisms have a critical consequence for thermalization between the $^3F_3$ and $^3H_4$ levels. We will first consider the case of quenching of the $^3H_4$ level. The rate-determining step for thermalization among these two excited levels is the non-radiative absorption connected to the rate $k_{nr}^{abs}(T)$, which competes with any decay pathway of the energetically lower $^3H_4$ level. Thus, if the total decay of the $^3H_4$ level is accelerated by additional multiphonon relaxation, the kinetically determined onset temperature, T_{on}, for Boltzmann thermalization between the excited states of Tm^{3+} increases even more. This is an expected fate in core-only nanocrystalline hosts with surface-attached ligands bearing functional groups with high vibrational energies. The other scenario of cross-relaxation quenching of the higher energetic $^3F_3$ level to the $^3F_4$ level generally depopulates the two relevant excited levels with no chance of phonon-assisted repopulation (ΔE $^3F_4 - {}^3H_4$ = 7000 cm^{-1}). This fate is expectedly rate-determining in core-shell nanocrystalline hosts, in which multiphonon relaxation related to the presence of the surface-attached ligands can be limited.

Overall, both quenching pathways for the excited $^3F_3$ and $^3H_4$ levels of Tm^{3+} pose severe limitations for the application of this lanthanide ion as a ratiometric (Boltzmann) UC nanothermometer, and even more specifically for the often targeted physiological temperature range (25-50 °C). Only in microcrystalline samples, when the Tm^{3+} contents is sufficiently low (to avoid any cross-relaxation effect), there is a chance to make use of UC ratiometric Boltzmann thermometry above 540 K with the two emission lines at 680 nm ($^3F_3 \rightarrow {}^3H_6$) and 800 nm ($^3H_4 \rightarrow {}^3H_6$) of Tm^{3+}. Because of the previously mentioned reasons, we have investigated an additional microcrystalline sample of $LiLuF_4$:1%Tm,30%Yb, prepared in a solid-state reaction, over a wide temperature range as a proof-of-concept. This synthesis route was selected as no ligands are used in the synthesis and therefore their consequent influence could be completely avoided. In the autoclave reaction, ligands can still be found on the particles surface. As can be concluded from the FTIR spectra (**Figure S15**), the solid-state microcrystalline sample is completely ligand-free.

View Article Online
DOI: 10.1039/D5TC01916H

The PL results are shown in **Figure S17** and **S18**. As expected, we observe Boltzmann-type behaviour above around 400 K indicating that the previously mentioned competing quenching pathways were successfully eliminated by completely avoiding ligand on the surface. Thus, the two excited $^3F_3$ and $^3H_4$ levels, and their mutual energy gap of $\Delta E_{21} \approx 1850\ \mathrm{cm^{-1}}$, can be employed for high-temperature thermometry in the optimum temperature range, described in Equation 3.[27]

$$T_{\mathrm{opt}} \in \left[\frac{\Delta E_{21}}{(2+\sqrt{2})k_{\mathrm{B}}}, \frac{\Delta E_{21}}{2k_{\mathrm{B}}}\right] = [758\ \mathrm{K}, 1294\ \mathrm{K}]$$

Equation 3

On the other hand, a fluoride host with a maximum cutoff phonon energy of around 500 $\mathrm{cm^{-1}}$ would not be advisable in this case as more than 3 cutoff phonon modes are required to bridge that large energy gap, which slows down the intrinsic non-radiative coupling strength $k_{\mathrm{nr}}(0)$ of these two excited levels ($^3F_3$ and $^3H_4$) by means of the energy gap law.[57] It has been demonstrated that the most advisable number of phonon modes should be either 1 or 2, if the intrinsic coupling is sufficiently strong such as in the case of Er^{3+}.[27,31] The reduced matrix elements for induced electric dipolar transitions, $\langle \|U^{(k)}\| \rangle^2$ (k = 2, 4, 6) for the electronic $^3F_3 \leftrightarrow {}^3H_4$ transition according to Carnall are $\langle \|U^{(2)}\| \rangle^2 = 0.0817$, $\langle \|U^{(4)}\| \rangle^2 = 0.3522$, $\langle \|U^{(6)}\| \rangle^2 = 0.2844$ implying an induced electric dipolar character for this transition.[36] The most critical competitive pathway to be avoided is multiphonon relaxation of the $^3H_4$ level.[36] Thus, aluminate garnet or vanadate ($\hbar\omega_{\mathrm{cut}}$ = 800 – 900 $\mathrm{cm^{-1}}$) hosts could be considered more advisable choices for Tm^{3+} if the two indicated excited levels are supposed to be exploited for ratiometric Boltzmann thermometry. Given a decay time of the $^3H_4$ level in the microcrystalline sample of around 1 ms, the expected onset temperature for Boltzmann behavior can be estimated by Equation 4:[27,58]

$$T_{\mathrm{on}} = \frac{\Delta E_{21}}{pk_{\mathrm{B}} \ln\left[1 + \left(\frac{g_2 k_{\mathrm{nr}}(0)}{k_{1\mathrm{r}}}\right)^{1/p}\right]}$$

Equation 4

With p as the number of involved phonons (here: p = 3 – 4), k_{B} as the Boltzmann constant, $k_{\mathrm{nr}}(0)$ as the intrinsic non-radiative coupling strength between the $^3F_3$ and $^3H_4$ level. The radiative decay rate of the $^3H_4$ level $k_{1\mathrm{r}}$ can be approximated as 1 $\mathrm{ms^{-1}}$, as shown in **Figure S18 (b)** . With the observation of $T_{\mathrm{on}} \approx (400 \pm 10)$ K, an intrinsic non-radiative coupling strength of $k_{\mathrm{nr}}(0) = (34.6 \pm 0.5)\ \mathrm{ms^{-1}}$ is roughly estimated. Such a low value would be expected for a thermalization involving three phonons but clearly demonstrates why Er^{3+} in β-$NaYF_4$ with a correspondingly faster intrinsic coupling strength between its green emitting $^2H_{11/2}$ and $^4S_{3/2}$ levels of $k_{\mathrm{nr}}(0) \approx 2\ \mu\mathrm{s^{-1}}$ offers a much wider dynamic working range in upconversion nanocrystals.[31] Thus, even if the high energy gap of Tm^{3+} would in principle promise higher relative sensitivities for a ratiometric luminescent thermometry concept, the high number of required phonons, the liability of the $^3H_4$ level towards non-radiative relaxation and the effective optimum performance range much above physiological conditions (see Equation 3) make Tm^{3+} an unsuited alternative candidate for physiological temperature sensing in the proposed manner. Another more general issue is the spectral range around 800 nm, which is difficult to access with high accuracy for photodetectors. Finally, the ratio $g_1 k_{\mathrm{nr}}(0)/k_{2\mathrm{r}} \approx 183$ makes the Judd-Ofelt allowed $^3H_4 \rightarrow {}^3H_6$-based emission (800 nm) much more intense compared to the $^3F_3 \rightarrow {}^3H_6$-based emission (680 nm). This clearly affects the overall expectable precision of such a conceptualized ratiometric thermometer, which ideally works with a $\Delta \approx 1$.[10] To investigate the influence of the surface better, different $LiLuF_4$:1% Tm^{3+}, X% Yb^{3+} @$LiYF_4$ core-shell NCs with X = 25, 30, and 35 were prepared and compared to the core counterparts. The photoluminescent emission maps and corresponding Δ are shown in **Figure 4** (e) and (f) for 1% Tm^{3+}, 30% Yb^{3+} and in **Figure S19** for the other Tm/Yb ratios. Here, no significant quenching of the $^3H_4 \rightarrow {}^3H_6$ electronic transition (800 nm emission) as well as an increase in intensity of the $^3F_{2,3} \rightarrow {}^3H_6$ electronic transition (680 nm emission) can be observed. This is what would be the expected behaviour for both transitions in terms of thermal quenching, as previously described in Equation 1 and 2.

Additionally, the general intensity was observed to be brighter than the core-only NCs. Decay curves and decay times for the respective core and core-shell NCs are shown in Figure 5 (d) and (e). The values of the decay times are also shown in **Table S3** in the SI. The decay times are all the same or higher than the core NCs

View Article Online
DOI: 10.1039/D5TC01916H

and MC counterparts. This indicates that the surface has a significant influence on both the nano- and microcrystalline samples, as no significant ion intermixing and consequent larger distances between the sensitizer and activator ion(s) were shown before. However, the interface region between the heterogeneous core-shell geometry is likely to induce local lattice distortions as well as the shell will shield the emissive ions in the core. Both of which will contribute to the different photoluminescence behaviour displayed.

To substantiate the previously explained model, also the influence of back energy transfer was investigated, in **Figure S20** and **Table S6**. PL emission maps and decay curves and decay times of the $LiLuF_4$: 1% Tm^{3+}, 30% Yb^{3+} MCs excited into the $^3H_4$ energy level (690 nm excitation) and observed at the $^2F_{5/2} \rightarrow {}^2F_{7/2}$ electronic transition of Yb^{3+}(1000 nm) are shown. They substantiate the previously discussed mechanisms of energy transfer, as Yb^{3+} shows the expected thermal deactivation. To exclude the possibility that the selected 30% Yb^{3+} is actually a too high concentration of activator and as a consequence easy energy migration to surface quenchers takes place, PL emission maps of $LiLuF_4$:1%Tm,20%Yb are shown in **Figure S21**. Also here, no Boltzmann behavior can be observed, substantiating previously discussed results.

Conclusions

In this work we considered the established Tm^{3+}, Yb^{3+} UC system for luminescent ratiometric thermometry regarding the emission lines of the $^3F_{2,3} \rightarrow {}^3H_6$ electronic transition (680 nm) and the $^3H_4 \rightarrow {}^3H_6$ electronic transition (800 nm) of Tm^{3+} and compare its performance to the well-established "working horse" example of the green-emitting Er^{3+}, Yb^{3+} UC system. We have selected $LiLuF_4$:1%Tm,30%Yb as a representative example in this work. Both micro- and nanocrystalline samples were considered to investigate the impact of surface-attached ligands with higher vibrational energies than the low cutoff phonon energies (~ 550 cm^{-1}) of the fluoride host itself. While the microcrystalline samples prepared by a solid-state reaction do indeed show Boltzmann behavior of the luminescence intensity ratio $\Delta = I_{680\ nm}/I_{800\ nm}$ above around 400 K and can be considered sensitive Boltzmann thermometers (S_r(450 K) = 1.32% K^{-1}), the nanocrystalline samples and microcrystalline samples with remaining surface ligands are not suited for luminescent thermometry at those temperatures. This observation can be related to the liability of the lower energetic $^3H_4$ level towards nonradiative multiphonon relaxation over ligands with high surface vibrational energies. In addition, the higher energetic $^3F_3$ level is prone to irreversible cross-relaxation at higher Tm^{3+} activator fractions. For effective luminescent thermometry at elevated temperatures with the Tm^{3+}, Yb^{3+} UC system, we advise selecting hosts with slightly higher cutoff phonon energies such as aluminate-based garnets or vanadates ($\hbar\omega_{\mathrm{cut}}$ = 800 – 900 cm^{-1}). Overall, however, the combination of experimental work on both micro- and nanocrystalline phosphors coupled with excited-state dynamics modelling helps substantiate that, in spite of the recorded success of the Tm^{3+}, Yb^{3+} couple for NIR-to-blue UC, Tm^{3+} cannot readily outperform the established lanthanoid ion Er^{3+} as a Boltzmann thermometer given the specific electronic energy level landscape of these two activators. This is of utmost importance to consider, as pushing the performance limits of the Er^{3+}–Yb^{3+} couple is still necessary for applications and the Tm^{3+}–Yb^{3+} pair was and still is heavily discussed as an alternative. This study demonstrates, however, that classic Boltzmann thermometry with the Tm3+ ion is not feasible for that purpose, especially within the physiological temperature regime.

Author contributions

M.L. was responsible for Investigation, Writing, Reviewing, Editing and Visualisation. **M.S.** was responsible for Investigation and Visualisation. **I.P.M.** was responsible for Investigation. **T.F.** was responsible for Investigation and Visualisation. **S.S.R.** was responsible for Investigation. **M.S**. was responsible for Investigation, Writing, Reviewing, Editing and Visualisation. **A.M.K.** was responsible for Conceptualization, Funding acquisition, Project administration, Supervision, Editing and Reviewing.

Conflicts of interest

There are no conflicts to declare.

Data availability

All raw data to the respective Figures presented in the manuscript is uploaded to a repository: **10.5281/zenodo.15187316.**

Acknowledgements

This work is part of a project that has received funding from the European Research Council (ERC) under the European Union's Horizon 2020 research and innovation program (Grant agreement No. 945945). Markus Suta is grateful for a scholarship by the "Young College" of the North-Rhine Westphalian Academy of Sciences, Humanities, and the Arts. The authors are indebted to Andries Meijerink for very helpful discussions.

Notes and references

1 M. Dramićanin, *Luminescence thermometry: Methods, materials, and applications*, Woodhead Publishing, an imprint of Elsevier, Duxford, United Kingdom, 2018.
2 L. D. Carlos and F. Palacio, Eds., *Thermometry at the Nanoscale: Techniques and Selected Applications*, The Royal Society of Chemistry, 2015.
3 D. Jaque Garcia and F. Vetrone, *Nanoscale*, 2012, 4301–4326.
4 M. Jia, X. Chen, R. Sun, D. Wu, X. Li, Z. Shi, G. Chen and C. Shan, *Nano Res.*, 2023. DOI:10.1007/s12274-022-4882-7.
5 B. Harrington, Z. Ye, L. Signor and A. D. Pickel, *ACS Nanosci. Au*, 2024, **4**, 30–61.
6 A. M. Kaczmarek, S. Abednatanzi, D. Esquivel, C. Krishnaraj, H. S. Jena, G. Wang, K. Leus, R. Van Deun, F. J. Romero–Salguero and P. Van Der Voort, *Microporous and Mesoporous Mater.*, 2020, **291**, 109687.
7 S. Premcheska, M. Lederer and A. M. Kaczmarek, *Chem. Commun.*, 2022, **58**, 4288–4307.
8 J. C. Martins, A. R. N. Bastos, R. A. S. Ferreira, X. Wang, G. Chen and L. D. Carlos, *Adv Photo Res*, 2021, 2000169.
9 N. Stopikowska, M. Runowski, P. Woźny, S. Goderski and S. Lis, *J. Lum.*, 2020, **228**, 117643.
10 C. D. S. Brites, R. Marin, M. Suta, A. N. Carneiro Neto, E. Ximendes, D. Jaque and L. D. Carlos, *Adv. Mater.*, 2023, **35**, 2302749.
11 C. D. S. Brites, S. Balabhadra and L. D. Carlos, *Adv. Opt. Mat.*, 2018, 1801239.
12 L. Đačanin Far and M. Dramićanin, *Nanomater.*, 2023, **13**, 2904.
13 B. M. Walsh, in *Advances in Spectroscopy for Lasers and Sensing*, eds. B. Di Bartolo and O. Forte, Springer Netherlands, Dordrecht, 2006, pp. 403–433.
14 M. Quintanilla, M. Henriksen-Lacey, C. Renero-Lecuna and L. M. Liz-Marzán, *Chem. Soc. Rev.*, 2022, 10.1039.D2CS00069E.
15 X. Qin, J. Wang and Q. Yuan, *Front. Chem.*, 2020, **8**, 608578.
16 A. Bednarkiewicz, L. Marciniak, L. D. Carlos and D. Jaque, *Nanoscale*, 2020, **12**, 14405–14421.
17 N. Jurga, M. Runowski and T. Grzyb, *J. Mater. Chem. C*, 2024, **12**, 12218–12248.
18 H. Fu, Y. Ma, Y. Liu and M. Hong, *Chem. Commun.*, 2021, **57**, 2970–2981.
19 A. Kar and A. Patra, *Nanoscale*, 2012, **4**, 3608.
20 R. Ghosh Chaudhuri and S. Paria, *Chem. Rev.*, 2012, **112**, 2373–2433.
21 H. Rijckaert and A. M. Kaczmarek, *Chem. Commun.*, 2020, **56**, 14365–14368.
22 T. P. Van Swieten, A. Meijerink and F. T. Rabouw, *ACS Photonics*, 2022, **9**, 1366–1374.
23 N. Stopikowska, P. Woźny, M. Suta, T. Zheng, S. Lis and M. Runowski, *J. Mater. Chem. C*, 2023, 10.1039.D3TC01684F.
24 C. Ma, X. Xu, F. Wang, Z. Zhou, D. Liu, J. Zhao, M. Guan, C. I. Lang and D. Jin, *Nano Lett.*, 2017, **17**, 2858–2864.
25 A. Ćirić, Ł. Marciniak and M. D. Dramićanin, *J. Appl.Phys.*, 2022, **131**, 114501.
26 J. Zhou, B. del Rosal, D. Jaque, S. Uchiyama and D. Jin, *Nat. Methods*, 2020, **17**, 967–980.
27 M. Suta and A. Meijerink, *Adv. Theory Simul.*, 2020, **3**, 2000176.
28 A. Bednarkiewicz, J. Drabik, K. Trejgis, D. Jaque, E. Ximendes and L. Marciniak, *Appl. Phys. Rev.*, 2021, **8**, 011317.
29 M. Runowski, P. Woźny, N. Stopikowska, I. R. Martín, V. Lavín and S. Lis, *ACS Appl. Mater. Interfaces*, 2020, **12**, 43933–43941.
30 A. M. Kaczmarek, M. Suta, H. Rijckaert, T. P. van Swieten, I. Van Driessche, M. K. Kaczmarek and A. Meijerink, *J. Mater. Chem. C*, 2021, **9**, 3589–3600.
31 M. Suta, *Nanoscale*, 2025, 10.1039.D4NR04392H.
32 Y. Zhu, S. Zhao, B. Zhou, H. Zhu and Y. Wang, *J. Phys. Chem. C*, 2017, **121**, 18909–18916.
33 J. Liu, H. Rijckaert, M. Zeng, K. Haustraete, B. Laforce, L. Vincze, I. Van Driessche, A. M. Kaczmarek and R. Van Deun, *Adv. Funct. Mater.*, 2018, **28**, 1707365.
34 M. Lederer, H. Rijckaert and A. M. Kaczmarek, *ACS Appl. Nano Mater.*, 2023, **6**, 2438–2449.
35 P. Huang, W. Zheng, S. Zhou, D. Tu, Z. Chen, H. Zhu, R. Li, E. Ma, M. Huang and X. Chen, *Angew. Chem.*, 2014, **126**, 1276–1281.
36 W. T. Carnall, H. Crosswhite and H. M. Crosswhite, *Energy level structure and transition probabilities in the spectra of the trivalent lanthanides in LaF_3*, 1978.
37 Y. Chang, H. Chen, X. Xie, Y. Wan, Q. Li, F. Wu, R. Yang, W. Wang and X. Kong, *Nat. Commun*, 2023, **14**, 1079.
38 H.-W. Chien, C.-H. Huang, C.-H. Yang and T.-L. Wang, *Nanomater.*, 2020, **10**, 2477.
39 N.-N. Dong, M. Pedroni, F. Piccinelli, G. Conti, A. Sbarbati, J. E. Ramírez-Hernández, L. M. Maestro, M. C. Iglesias-de la Cruz, F. Sanz-Rodriguez, A. Juarranz, F. Chen, F. Vetrone, J. A. Capobianco, J. G. Solé, M. Bettinelli, D. Jaque and A. Speghini, *ACS Nano*, 2011, **5**, 8665–8671.
40 I. N. Bazhukova, V. A. Pustovarov, A. V. Myshkina and M. V. Ulitko, *Opt. Spectrosc.*, 2020, **128**, 2050–2068.
41 B. Yang, H. Chen, Z. Zheng and G. Li, *Jour. Lum.*, 2020, **223**, 117226.
42 D. Gao, Y. Liang, J. Gao, H. Xin, L. Wang, S. Yun and X. Zhang, *Jour. Lum.*, 2021, **238**, 118261.
43 B. Bendel and M. Suta, *J. Mater. Chem. C*, 2022, 10.1039.D2TC01152B.
44 M. Misiak, O. Pavlosiuk, M. Szalkowski, A. M. Kotulska, K. A. Ledwa and A. Bednarkiewicz, *Nanotechnology*, DOI:10.1088/1361-6528/acd701.
45 D. V. Pominova, V. Y. Proydakova, I. D. Romanishkin, A. V. Ryabova, P. V. Grachev, V. I. Makarov, S. V. Kuznetsov, O. V. Uvarov, V. V. Voronov, A. D. Yapryntsev, V. K. Ivanov and V. B. Loschenov, *Laser Phys. Lett.*, 2020, 13.
46 H. Suo, P. Zhao, X. Zhang, Y. Guo, D. Guo, J. Chang, J. Chen, P. Li, Z. Wang, H. Wei, W. Zheng and F. Wang, *Nat. Commun*, 2025, **16**, 3249.
47 Y. Zheng, H. Xu, X. Xu, L. Xu, S. Wang and S. Wu, *Jour. Alloys Compd.*, 2022, **910**, 164778.
48 A. M. Kaczmarek, R. Van Deun and M. K. Kaczmarek, *Sens. Actuators B: Chemical*, 2018, **273**, 696–702.
49 L. Giordano, M. Nunes, V. Teixeira and L. Rodrigues, *J. Braz. Chem. Soc.*, DOI:10.21577/0103-5053.20210052.
50 X. Zhai, P. Lei, P. Zhang, Z. Wang, S. Song, X. Xu, X. Liu, J. Feng and H. Zhang, *Biomaterials*, 2015, **65**, 115–123.

View Article Online
DOI: 10.1039/D5TC01916H

51 O. Savchuk, J. J. Carvajal Marti, C. Cascales, P. Haro-Gonzalez, F. Sanz-Rodríguez, M. Aguilo and F. Diaz, *Nanomaterials*, 2020, **10**, 993.
52 N. J. J. Johnson, S. He, S. Diao, E. M. Chan, H. Dai and A. Almutairi, *J. Am. Chem. Soc.*, 2017, **139**, 3275–3282.
53 M. Lin, Y. Zhao, S. Wang, M. Liu, Z. Duan, Y. Chen, F. Li, F. Xu and T. Lu, *Biotechnol. Adv.*, 2012, **30**, 1551–1561.
54 X. Jiang, C. Cao, W. Feng and F. Li, *J. Mater. Chem. B*, 2016, **4**, 87–95.
55 Z. Wang, J. Christiansen, D. Wezendonk, X. Xie, M. A. Van Huis and A. Meijerink, *Nanoscale*, 2019, **11**, 12188–12197.
56 S. A. Burikov, O. E. Sarmanova, A. A. Fedyanina, I. V. Plastinin and T. A. Dolenko, *Spectrochim. Acta A: Mol. Biomol. Spectr.*, 2025, **334**, 125902.
57 L. A. Riseberg and H. W. Moos, *Phys. Rev.*, 1968, **174**, 429–438.
58 T. P. Van Swieten, J. M. Steenhoff, A. Vlasblom, R. De Berg, S. P. Mattern, F. T. Rabouw, M. Suta and A. Meijerink, *Light Sci Appl*, 2022, **11**, 343.

View Article Online
DOI: 10.1039/D5TC01916H

Data availability

All raw data to the respective Figures presented in the manuscript is uploaded to a repository:

10.5281/zenodo.15187316.